# Angstrom-Resolved Real-Time Dissection of Electrochemically Active Noble Metal Interfaces

Buddha R. Shrestha, Theodoros Baimpos, Sangeetha Raman, and Markus Valtiner*

Department for Interface Chemistry and Surface Engineering, Max-Planck-Institut für Eisenforschung GmbH, Max-Planck-Straße 1, D-40237 Düsseldorf, Germany

ABSTRACT Electrochemical solid|liquid interfaces are critically important for technological applications and materials for energy storage, harvesting, and conversion. Yet, a real-time Angstrom-resolved visualization of dynamic processes at electrified solid|liquid interfaces has not been feasible. Here we report a unique real-time atomistic view into dynamic processes at electrochemically active metal interfaces using white light interferometry in an electrochemical surface forces apparatus. This method allows simultaneous deciphering of both sides of an electrochemical interface—the solution and the metal side—with microsecond resolution under dynamically evolving reactive conditions that are inherent to

technological systems *in operando*. Quantitative *in situ* analysis of the potentiodynamic electrochemical oxidation/reduction of noble metal surfaces shows that Angstrom thick oxides formed on Au and Pt are high-*ik* materials; that is, they are metallic or highly defect-rich semiconductors, while Pd forms a low-*ik* oxide. In contrast, under potentiostatic growth conditions, all noble metal oxides exhibit a low-*ik* behavior. On the solution side, we reveal hitherto unknown strong electrochemical reaction forces, which are due to temporary charge imbalance in the electric double layer caused by depletion/generation of charged species. The real-time capability of our approach reveals significant time lags between electron transfer, oxide reduction/oxidation, and solution side reaction during a progressing electrode process. Comparing the kinetics of solution and metal side responses provides evidence that noble metal oxide reduction proceeds *via* a hydrogen adsorption and subsequent dissolution/redeposition mechanism. The presented approach may have important implications for designing emerging materials utilizing electrified interfaces and may apply to bioelectrochemical processes and signal transmission.
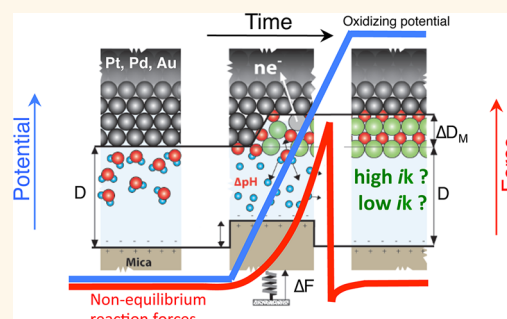
KEYWORDS: electrochemisty · oxide growth · noble metals · corrosion · catalysis · optical properties

Structure and dynamics at electrochemical solid|liquid interfaces drive functionality, stability, and capabilities in a wide range of important technologies such as batteries,[1] supercapacitors,[2] fuel cell catalysts,[3-5] electrochemical hydrogen generation,[6] and corrosion[7] phenomena. Under operation conditions, electrochemical potentials at electrodes may vary and cycle strongly, giving rise to the formation of metal oxide films and/or their reduction, promoting material degradation. Hence, the mechanism of electrochemical oxidation and reduction of metals is fundamental to the understanding of interfacial electrochemical processes such as corrosion and noble metal catalysis and has been the focus of numerous studies over the last decades.[8-11] State-of-the-art methods and means to investigate active electrochemical interfaces during oxidation/reduction cycling

separately investigate either the solution or the metal side of the interface. Recent exciting developments providing a more detailed view into the dynamics of electrochemical processes focus on collecting solution side products (solutes such as ions and gases) of an electrode process by combination of a scanning flow cell with inductively coupled plasma mass spectroscopy[12-18] and channel flow double electrodes.[19-21] Likewise, electrochemical quartz crystal microbalance (EC-QCM)[22] provides detailed information about mass changes of the metal electrode during potential cycling. Although motivated by the health and economic impact of corrosion[23] and the ever-increasing energy consumption of our societies, the almost 5 decades old problem to *in situ* monitor electrochemical interfaces on the atomistic scale in real time is still unsolved. *In situ* electrochemical scanning tunneling microscopy (STM), atomic force
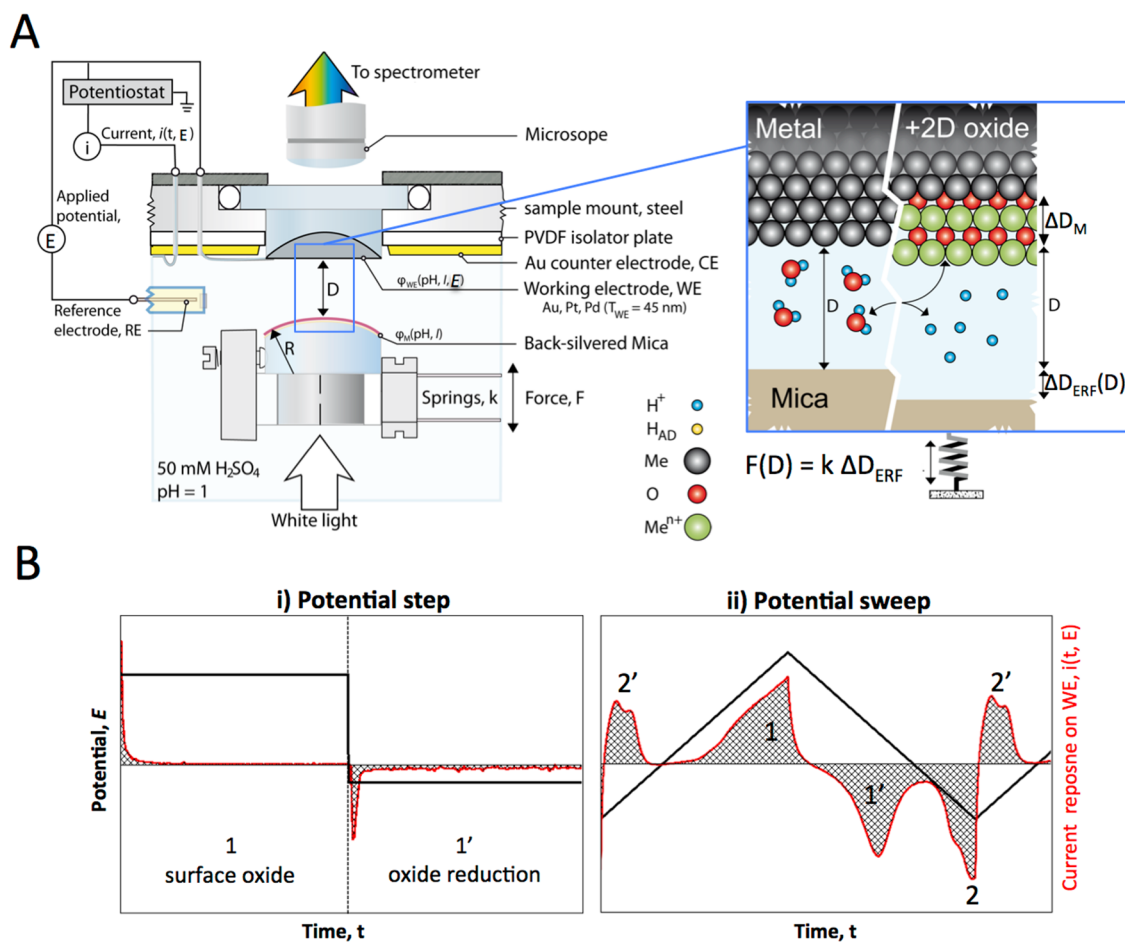
Figure 1. (A) Schematic of the electrochemical SFA setup. The small inset details experimental observables. (B) Typical current *versus* time profile of (left) a potential step and (right) a cyclic voltametry experiment indicating electrochemical processes such as surface oxide film growth/reduction (1/1′) and hydrogen adsorption/desorption (2/2′) (cf. text for details).

microscopy (AFM), and X-ray diffraction provided very detailed understanding of steady-state oxide structures,[24−27] ion layering,[28] and passivation[29] at electrodes. However, time resolution still limits the investigation of active interfaces. In particular, consider, for instance, an active surface oxidation or reduction reaction that proceeds within, at most, a few seconds, and hence subsecond dynamics at an electrochemically active interface are fundamental to electrocatalysis, corrosion, and materials for energy harvesting.

The *in operando* concomitant assessment of qualitative and quantitative structural and dynamic aspects of both the solution side and the metal side of an electrochemical interface has not been feasible to date. Recently, we developed an electrochemical (EC) attachment to the surface forces apparatus (SFA)[30−32] and applied templating techniques to generate molecularly smooth gold (Au) films for use in the EC-SFA.[30−32] Here we extend these techniques to noble metals (platinum and palladium) and visualize and quantify electrochemical metal oxidation, reduction, and the solution side equilibration in real time. Figure 1A shows the schematic of the EC-SFA setup. An atomically smooth mica surface, which is coated at the backside with a

semitransparent 45 nm thick Ag layer, is facing a molecularly smooth metal mirror (Au, Pt, or Pd) in 50 mM aqueous H_2SO_4 solution. The distance, D, between the two opposing surfaces can be measured and controlled with sub-Angstrom accuracy using white light multiple beam interferometry (MBI).[33] Simultaneously, electrochemical potentials and currents can be controlled at the metal mirror working electrode (WE),[30] and any force acting between the surfaces is measured by a spring (spring constant, k) to which the apposing surface is mounted.

RESULTS AND DISCUSSION

Here we use a novel experimental EC-SFA protocol—electrochemical *MBI at constant separation*— to study in detail an active electrochemical process under both equilibrium and nonequilibrium conditions. For this method, the reflecting working electrode surface (Au, Pt, and Pd) is placed facing the back-silvered mica surface at controlled and fixed "mechanical" separation, and the absolute "optical" distance D between the electrochemical interface and an opposing inert surface is measured using MBI as previously described.[33] An additional schematic of the interferometer is shown in Supporting Information (Figure S2).
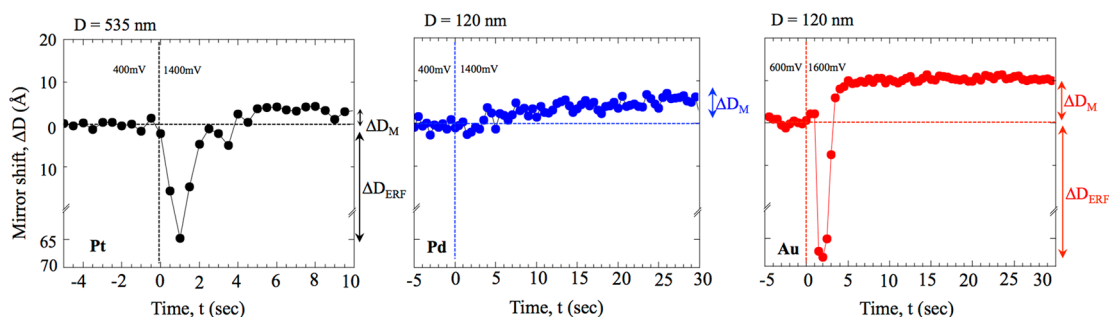
Figure 2. Distance shift ΔD during potentiostatic oxidation experiments recorded in 50 mM H_2SO_4 for Pt, Pd and Au. Shifts of ΔD_{ERF} due to electric double layer depletion forces and ΔD_M due to metal mirror shifts caused by surface oxidation are indicated. These contributions to ΔD can be clearly distinguished based on their distance and time dependence.

As shown in Figure 1A, we use MBI to monitor the time-dependent change ΔD of the absolute optical distance D at constant mechanical separation, while electrochemical signals such as cyclic voltammograms or potentiostatic step experiments (stepping between two set electrochemical potentials E) are imposed on the metal working electrode (Figure 1B). This allows inducing electrochemical processes such as surface oxidation (1 in Figure 1B) and reduction (1′ in Figure 1B) or ion desorption and adsorption (2 and 2′ in Figure 1B). Simultaneously, one can record the shift of the WE metal mirror ΔD_M caused by interfacial electrochemical reactions and electrochemical currents passing through the WE interface. The opposing mica surface is not involved in any active reactions and acts as a scanning probe surface, providing the opposing mirror (at the backside and sealed from solution) to utilize MBI. In addition, this surface is mounted to a spring and is hence capable of sensing the solution side response of the working electrode, that is, a change of the electric double layer, in terms of measurable displacements ΔD_{ERF} and hence forces $F(D) = k\Delta D_{ERF}$ acting between the probe surface and the electrochemical interface (the subscript ERF denotes electrochemical reaction force).

The inset in Figure 1A further details the experimental observables. Any resulting shift of the position (ΔD) caused by the actively progressing reactions at the interface is recorded with frame rates ranging up to 50 frames per second. A measured ΔD can be directly related to the sum of a shift of the reflecting metal surface ΔD_M and an electrochemical reaction force (ERF) $F_{ERF}(D) = k\Delta D_{ERF}$ acting between the mica probe surface and the metal mirror WE. Forces $F(D)$ are distance-dependent and can be easily identified by increasing the working distance D. Any interaction force decays with increasing D, and a plot of the force ($F_{ERF}(D) = k\Delta D_{ERF}$) as a function of D reveals the force law of any nonequilibrium forces during an active process. Shifts in ΔD_M of the metal mirrors due to electrochemically induced changes such as consumption of and/or deposition of reflecting layers on the electrochemically active metal mirror result in absolute and real-time measured translations of the reflecting

interface. For instance, as shown in Figure 1A (right), if metal is consumed and transformed into a transparent oxide, the reflecting metal is shifted by ΔD_M as indicated. Such a shift is not distance-dependent and thus clearly distinguishable from an acting force. The optical analysis of ΔD_M provides a very accurate measure of the optical properties of interfacial chemistry changes. In essence, this method is complementary to spectroscopic ellipsometry,[34] which analyzes reflected light, while here we analyze light transmitted through an interferometer. In addition, our method allows simultaneous study of both the metal and the solution side of an electrochemical interface in real time with microsecond time resolution under dynamically evolving conditions.

Using the setup shown in Figure 1, we studied in real time both dynamic and static oxidation and reduction of Au, Pt, and Pd noble metal surfaces, that is, the electrochemically driven formation/breakdown of only a few atomic layer thick metal oxides.

Figure 2 shows the optical mirror shift ΔD during potentiostatic oxidation of Pt, Pd, and Au surfaces. The reduction is shown in the Supporting Information (see Figure S3). The results of these experiments reveal interesting differences between the different metal surfaces. First, Pt and Au oxidation proceeds quickly within about 5 s, forming a stable steady-state passivating oxide film while the Pd oxidation proceeds gradually. The converged metal mirror shift ΔD_M after oxidation is 2.5 ± 0.6, 9 ± 0.6, and 10 ± 0.6 Å for Pt, Pd, and Au, comparing well with 1, 3, and 3 times the monolayer (ML) thickness of the metal. For Pt, it is straightforward to calculate the real electrochemically active area using the hydrogen adsorption peaks (assuming 210 μC cm^{-2} of charge per hydrogen ML) in the cathodic potential region. This allows giving an accurate measure of the ML consumption based on transferred charges. For the experiment shown in Figure 2, we calculate 0.9 ML of metal consumption for Pt, which compares well with the EC-SFA data.

In addition to ΔD_M, we observed a large negative distance shift $\Delta D = \Delta D_{ERF}$ (see again Figure 2) within the first few seconds of the oxidation process of
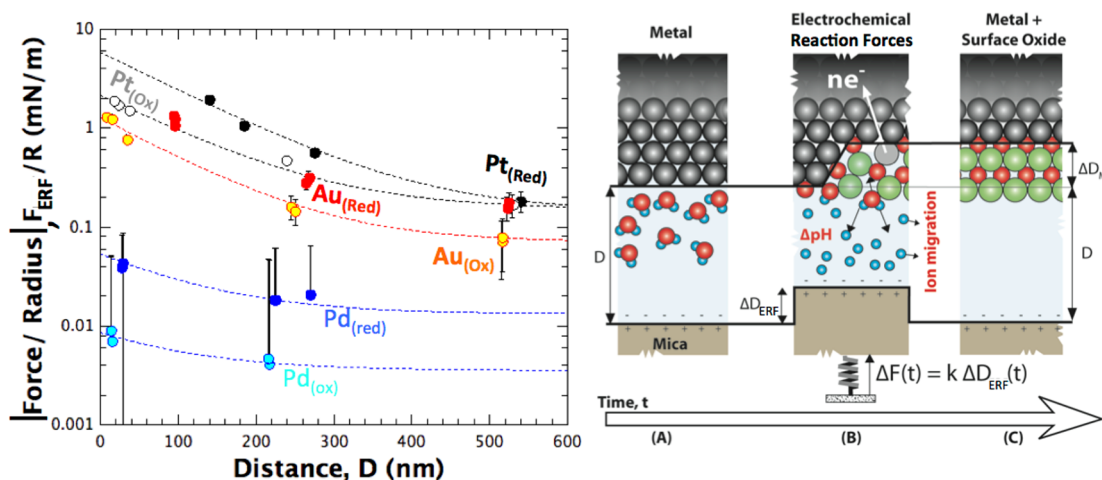
Figure 3. Electrochemical depletion forces measured in 50 mM H_2SO_4 while performing potential step experiments, shown in Figure 2. Forces measured during oxidation are attractive (*i.e.*, negative) but plotted positive in this semilog plot. Dotted lines indicate fitting of the data (cf. text for details); parameters are given in Table S2. Lower error bars going below zero for very low measured forces are not shown. The schematic details the interface depletion during oxidation. The charging of the EDL on the apposing mica surface is indicated (cf. Figure S3 for a schematic detailing the depletion during reduction).

both Au and Pt electrodes. ΔD_{ERF} is due to injection/consumption of charge at the interface that manifests itself in a measurable force and hence translation of the optical distance D. In particular, during an oxidation process at a metal anode, a typical electrochemical half-reaction proceeds as follows:

$$n\text{Me} + m\text{H}_2\text{O} \leftrightarrow \text{Me}_n\text{O}_m + 2m\text{H}^+ + 2m e^- \qquad (1)$$
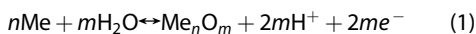
Hence, during an oxidation process, protons are released into the anode interface. This leads to an instantaneous charge imbalance within the electric double layer (EDL), which does not obey electroneutrality during the ongoing active electrochemical process. The force generated by this electrostatic imbalance manifests in the observed ΔD_{ERF} that is both time- and distance-dependent. As such, ΔD_{ERF} directly correlates with the solution side release of protons (or *vice versa* depletion during reduction) into (from) the electric double layer. Interestingly, ΔD_{ERF} increases to a maximum at about 2 s after maximum charge injection (see current transients in Supporting Information Figure S8) and decays 1−2 s after the completion of the charge injection. Hence, the solution side equilibration is considerably shifted in time by 2 s compared to the electrochemical electron transfer process, maintaining a large field at the electrode interface until full solution side equilibration.

Figure 3 shows the force $F_{ERF}(D,t) = k\Delta D_{ERF}(t,D)$ measured at the time t of the maximum solution side response. The force experienced during oxidation is attractive yet plotted as absolute number on a semilog scale (negative ΔD indicates an attractive force). The measured distance-dependent force profile seen in Figure 3 can be fit well with a consistent set of parameters (see Table S2 for details) using an interaction potential of $W(D) = W_0\exp(-D/\Delta\lambda_{ERF}) + C$ and Derjaguins approximation[35] with the empirical

pre-exponential factor W_0 and the effective nonequilibrium screening length $\Delta\lambda_{ERF}$.

Hence, ERF decays exponentially as a function of the distance toward a constant value. This constant can be understood in terms of the unscreened nonequilibrium electric field between the metal working electrode and the counter electrode during active reaction progress. Similar to a capacitor, the field from the anode to the cathode (where the counter reaction to reaction 1 proceeds) decays linearly, and hence the force is constant and independent of the distance D. The exponential term of the equation can be intuitively understood similar to the decay length within plasmas. Evolving charge forms a Boltzmann distributed layer at the electrode at any instance in time during an active process. Interestingly, $\Delta\lambda_{ERF} = 100-110$ nm is up to 2 orders of magnitude larger compared to the expected equilibrium decay (or screening) length, the so-called Debye length $\Delta\lambda_D = 7.8$ Å within the used electrolyte. This is due to the uncompensated electrostatic repulsions. Interestingly, ERF magnitudes measured at Pd electrodes are much weaker compared to Pt and Au. This can be rationalized in terms of the kinetics of the oxide growth. As already mentioned and displayed in Figure 2, the oxide on Pd grows slower (see transient curves in Figure S8), and hence the charge imbalance generated in similar time intervals is much lower.

A qualitatively similar behavior was observed during reduction, which is the reverse of reaction 1. Figure 3 also shows ERF during reduction in a potentiostatic step experiment (see also Figure S3 in the Supporting Information) measured at the maximum of the experience force. Here, ERF during reduction is repulsive. During reduction, protons are consumed, leading to an excess negative charge at the active electrode, resulting in an electrostatic repulsion with the sulfate ions at

the mica probe surface. It is interesting to note that the absolute magnitude of the measured ERF is about a factor of 2−3 higher compared to the anodic oxide growth, while the decay length is similar. The higher magnitude scales with the reaction rate (see current *versus* time data in Figure S8), with faster rates resulting in higher forces. Again Pd displays much lower forces, which cannot be attributed to slower reduction kinetics in the case of the reduction process. All metals reduce with similar kinetics with most of the charge transfer occurring within the first second (Figure S8).

In fact, during reduction, the charge imbalance due to depletion of positive charge can be compensated not only by electromigration of charged solution species but likewise by dissolution of positive metal ions into the interface. In particular, Pt and Au have much lower dissolution rates compared to Pd,[19−21] which correlates well with the measured magnitudes of ERF. It can be expected that the magnitude of the solution side response will be larger if depleted protons are not replaced by dissolution of positively charged metal ions. Hence, on Pd electrodes that show more significant dissolution during reduction,[20] the measured ERF is considerably lower through charge compensation by ion transfer from the metal surface into solution. In other words, the potential that is built up temporarily at the active interface acts as a strong (electrostatic) driving force promoting dissolution of even the noblest metals as ions into the depleted solution during an active reduction process. Reductive dissolution is a major degradation mechanism observed for electrocatalysts.[13−15,17,19−21]

In summary, ERF can be attractive or repulsive depending on the charge of the electrochemically generated/consumed species and the EDL on the opposing probe surface. In the present case, forces are attractive during oxidation (proton evolution) and repulsive during reduction (proton consumption/ depletion), correlating with the opposing electric double layer at the positively charged mica probe surface side that is made up from sulfate ions. ERF magnitudes at close separation distances can range up to $W_0 \sim 10$ mN/m and are hence capable of overpowering typical van der Waals forces and electric double layer forces, which have similar orders of magnitude at very close separation distances in aqueous electrolytes. Hence, repulsive ERF may contribute to particle detachment of fuel cell catalysts from support materials,[36,37] as well as to the initiation of crack propagation in confined environments (crevices/stress corrosion cracks) where the observed forces will always be repulsive with considerably higher magnitudes. In particular, both sides in confinement situations are typically symmetric (*i.e.*, similar) and simultaneously deplete/load the interface with like charges. Together with a much slower diffusion and migration kinetic in confined spaces, the

accumulation of like charge and hence ERF can be expected to be much higher in confinement.

In addition to these static experiments, the developed approach allows one to also look into dynamically changing systems, which are ultimately important in technological applications. For Pd and Pt (Au is displayed in Figure S7; see Supporting Information) surfaces, Figure 4 compares the electrochemical current with the measured optical shift ΔD as a function of time while applying a triangular wave potential with a constant rate of 50 mV/s. The mirror shift is displayed for distances $D > 140$ nm, where potential ERF forces are relatively small, as indicated. The maximum distance shifts expected due to forces under maximum reaction progress range from about $\Delta D_{ERF} = F(D)/k = 5 − 15$ Å from Pd to Pt and are at these large distances only visible around the maximum solution side responses during reduction. These manifest as peaks in the $\Delta D(t)$ plots shown in Figure 4. ERF force distance profiles during dynamic experiments are discussed in detail in the Supporting Information. Within 0.5−2 s prior and past these solution side peaks, ERF is not detectable at the given large distances allowing the direct extraction of ΔD_M. In addition, using the ΔF_{ERF}- (D) allows discrimination between force effects and real optical shifts of the reflecting interface.

Surprisingly, in dynamic experiments, both Pt and Au (Au data are displayed in Figure S7) experiments reveal a negative shift of the distance ΔD_M during the anodic scans toward higher applied electrochemical potentials. This corresponds to an outward shift of the reflecting interface in this experimental setup as indicated in the schematic in Figure 4. Hence, Pt and Au metal oxide films are not transparent under dynamic conditions. The absorption coefficient (*i.e.*, the imaginary part ik of the refractive index) is high and within the range characteristic for metals or defect-rich semiconductors. This compares well to data from spectroscopic ellipsometry.[11] Moreover, from the data, it is clearly evident that the optical properties of the oxide films change upon reversal of the potential. The mirror shifts back to positive values of 0 Å for Pt and 3−4 Å for Au (Figure S7). A persisting current accompanies this shift of the reflecting mirror immediately after reversal of the potential. From the results, one can deduce a very important and interesting insight: As discussed earlier and shown in the schematic in Figure 4, a positive shift $\Delta D_M > 0$ of the mirror indicates a transparent oxide with an essentially zero absorption coefficient ik. For Pt electrodes, the shift associated with reversing the potential results in a zero shift compared to the reflections under condition where no oxide film is present. This is only consistent with a phase transformation toward an oxide phase consisting of a two-layered Pt oxide with one high-ik layer and one low-ik layer, sitting on top of the high-ik phase. This layer is made up from 1 ML of metal, which also agrees well with
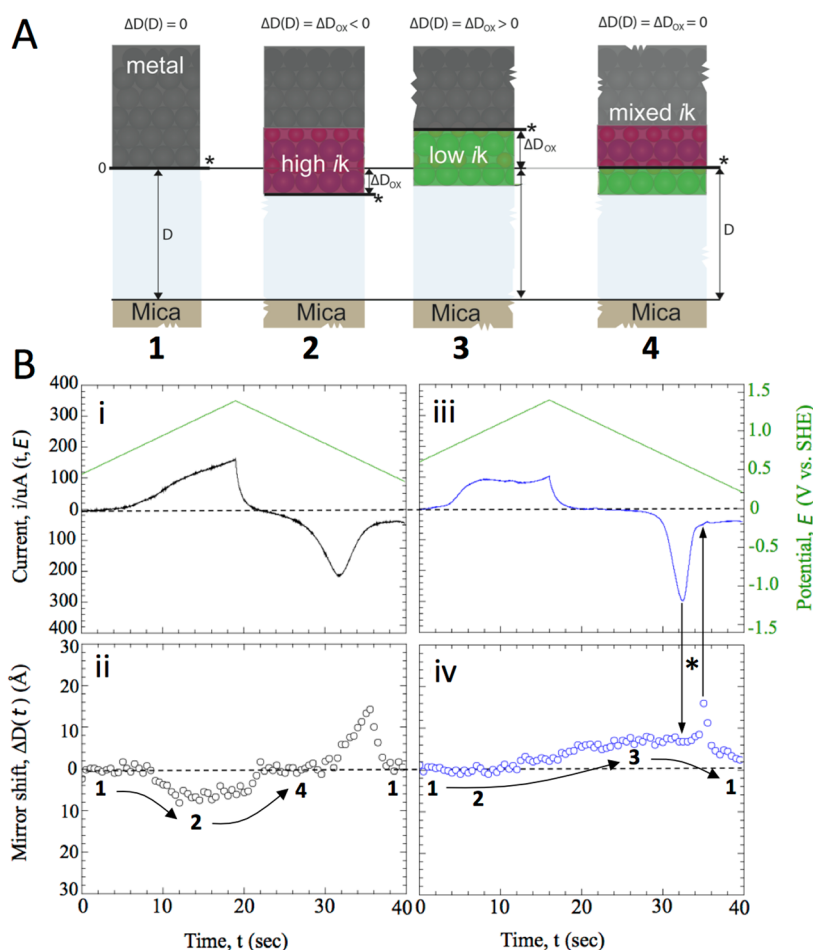
Figure 4. (A) Schematic of different possible resulting mirror shifts on a metal surface (1) due to growth of (2) a high-*ik* oxide structure, a (3) low-*ik* and thus transparent oxide structure, or (4) a mixed two-layer structure consisting of both a low- and a high-*ik* phases, effectively resulting in zero mirror shift. The reflecting interfaces are marked with an asterisk (cf. text for details). (B) Cyclic voltammogram, potential ramp, and resulting mirror shifts $\Delta D(t)$ due to potentiodynamic cycling of the applied potential E in 50 mM H_2SO_4 for Pt (i and ii) and Pd (iii and iv), respectively. Potential explanations for the mirror shift are indicated and refer to (A).

the EC-estimated Pt oxidation of 0.9 ML as well as static experiments. In addition, our simulations (shown in Figure S2b) indicate that an oxide with $ik = 2$ effectively leads to a net zero shift ΔD_M. Similarly, Au electrodes (shown in the Supporting Information Figure S7) display a positive ΔD_M shift to 3−4 Å upon reversing the potential, indicating a phase transformation or filling of electronic defects of the oxide structure. Using measured current and the geometric area and assuming an oxide consisting of Au^{2+} estimates 1.7 monolayers of metal consumption, which compares well with the measured $\Delta D_M = 3−4$ Å after reversal of the potential or about 1.5−1.7 ML of gold consumption (ccp unit cell: $a = 4.08$ Å and $n = 2$) and literature.[38,39]

In contrast to Au and Pt, the Pd case shows a generally expected behavior with a metal mirror shift of $\Delta D_M = 5.5$ Å upon full oxidation of the metal surface, or three monolayers of consumed metal (as compared to 2.1 monolayers using the electrochemical current density). It is noteworthy that the optical result is

independent of the real electrode area, a significant problem for calculations of oxide thicknesses based on consumed charge densities. This positive shift indicates the formation of a transparent metal oxide with a low absorption coefficient ik. Hence, the measured shift directly reflects the consumption of three monolayers of the metallic substrate and its transformation into a transparent metal oxide with a low imaginary part of the refractive index ik. This experiment can thus directly quantify the amount of metal that is transformed into an oxide during active cycling. Interestingly, the oxidation of Pd shows an initial small but significant drop to negative distances $\Delta D_M = -1$ Å for about 5 s, although a significant charge was already injected. This ΔD_M drop is followed by constant growth (constant slope) of the oxide at higher applied potentials. After reversing the potential and once the current falls below zero, the measured mirror shift remains constant at 5.5 Å, indicating that oxide growth stopped at about three monolayers. The initial slightly negative ΔD_M and

the consecutive constant slope toward the fully formed oxide layer indicate the initial formation of a high-ik oxide, followed by growth of a transparent low-ik oxide. This behavior is fully consistent with the proposed place exchange mechanism[22] that results in growth of thicker oxide films as a high-field mechanism.[9] The final ΔD_M measured for Pd is similar, compared to the potentiostatic experiment.

Surprisingly, the dynamic growth of an oxide on Au or Pt is much different compared to the static case. Apparently, the growth mechanism of an oxide due to an instant jump of the potential (to an oxidizing potential) and subsequent equilibration may result in completely different oxide structure compared to a dynamic oxide growth under nonequilibrium conditions. In further support of the presented conclusions and in order to estimate effects of phase changes,[40] we show additional simulations of expected "optical" distance changes ΔD_M due to growth of metal oxides of different thicknesses and optical properties (high- or low-ik) using the transfer matrix method[41] as implemented in Reflcalc[34,42,43] in section B of the Supporting Information.

Figure 4 (iii and iv) also provides direct real-time insight into the different kinetics of current injection, solution side response, and equilibration as well as oxide reduction. As marked in the plot, on the cathodic sweep, the measured ΔD_{ERF} exponentially rises toward a maximum, which is 2 s after the maximum current passed through the WE and just after completion of the electrochemical electron transfer reaction. First, this indicates that the solution side migration of protons toward the interface is not a rate-limiting step in the electrochemical reaction pathway, as solution side equilibration exhibits a 2 s time lag compared to electron injection. Furthermore, as can be seen from F_{ERF} plots taken at distances very close to the interface (see Figure S5), the rise of the solution side ERF progressively starts with the current injection. This is a clear indication of proton depletion at the solution side due to a continuous adsorption of hydrogen on the thin oxide film. Moreover, as can be seen (marked by asterisk), even when charge is injected with maximal rate, the metal mirror is not yet re-established at the initial zero position. About 2 s after charge injection, the solution side response is maximal and the metal mirror is becoming re-established (i.e., ΔD_M approaches zero). This behavior is consistent with a complex dissolution/redeposition mechanism during reduction.[16] The larger reductive ERF present during the reduction currently prevents us from clearly resolving the re-establishing of the metal mirror kinetics on Pt and Au. The maximum solution side response is however similarly shifted by about 2 s compared to the maximum of the charge injection (see Supporting Information Figure S5) and may indicate a similar

mechanism. In Figure 2, a similar behavior can be observed for potentiostatic experiments.

It is interesting to note that the time-dependent potential/force profile of ERFs (shown in Supporting Information Figure S5) resembles the typical profile of an action potential,[44] as observed for synapse signal release. An exponential increase of the measured potential (force), followed by an instant collapse back to the initial rest potential of the surface indicates a process with a positive feedback loop with respect to the proton consumption. The more protons react during the reduction reaction, the more alkaline the interface becomes and the more anions are uncompensated within the EDL. This can effectively change the activation barriers of electrochemical and dissolution reactions due to EDL effects.[45] Once the oxygen atoms are fully released from the oxide, the surface potential drops to an equilibrium value and consumed protons will be replenished by proton migration/hopping toward the electrochemical interface.[35] In summary, from these measurements, we conclude that the reduction mechanism of the oxide proceeds via two steps, a rate-limiting first hydrogen adsorption, followed by a subsequent dehydration of the hydrogen covered or hydrogen-rich (in terms of the chemical potential of hydrogen[46]) metal oxide. Re-establishing of the metallic surface state does not necessarily coincide with the amount of injected current—a significant insight into electrochemical oxide reduction complementing information from other techniques such as EC-QCM.[22]

CONCLUSIONS

In conclusion, EC-SFA can reveal unprecedented insights in both the solid as well as the solution side of an electrochemical interface, providing a unique in situ Angstrom-resolved and real-time visualization of electrochemically active interfaces. As an optical method, it is nondestructive and allows characterizing metal oxides, their oxidation and reduction kinetics, and in particular the kinetics and characteristic time lags between solution side and electrode side equilibration during active electrochemical processes. This allowed providing experimentally further evidence to understand the mechanism during reduction of a few Angstrom thin 2D oxide films on noble metals. The hitherto unknown electrochemical reaction force, which can be attractive or repulsive, may significantly contribute to degradations observed in many material systems ranging from fuel cell catalysts to crevice corrosion and stress corrosion cracking. Likewise, ERF and generally reactive forces may also be fundamentally important to structure and functionality in biological and nanoconfined systems.[47,48] Hence, the newly developed approach and results may also be valuable for studying active

interfaces in a number of different fields, ranging from ion release reactions at cell membranes and charge transfer across lipid bilayers to nanofluidics and MEMS, where similar nonequilibrium effects may be used to drive and control structure and functionality.

METHODS

Chemicals and Materials. All chemicals were obtained from Sigma-Aldrich and used to make a solution of 500 mM H_2SO_4 (0.5 mol/L). The 50 mM H_2SO_4 solutions, used in the current experiment, were prepared from 500 mM H_2SO_4 (0.5 mol/L). Water used in the experiments was deionized using a Milli-Q filtration system (resistivity ≥ 18.2 M$\Omega \cdot$cm and TOC ≤ 2 ppb). Noble metals were purchased from GoodFellow (Au, 99.99%; Pt, 99.95%; and Pd, 99.95%). Atomically smooth noble metal films on SFA discs were prepared by template stripping of metal films deposited on an atomically smooth mica surface[30] using an electron-beam PVD at base pressures below 3×10^{-6} mbar. Deposition rates of the metals onto mica were kept below 1 Å/s. Preparation of the opposing atomically smooth mica surfaces was performed as previously described.[30] Surface roughness of the surfaces was checked prior to and after experiment and revealed an rms roughness below 8 Å for all metals with little changes due to electrochemical treatment (see Supporting Information Figure S1). In particular, the EC-SFA measurement averages over an area of about 1 μm $\times$ 10 μm, where nanoscale roughness is effectively canceled for any zero calibration at large distances. Hence, surface roughness does not play a role in the absolute mirror shift at large separation, while at small separations (on the order of the rms roughness) and in contact, a constant ΔD shift scaling with the rms roughness is found.[30−32]

EC-SFA Measurements. The electrochemical three-electrode attachment consists of a noble metal working electrodes, a Au counter electrode, as well a Ag|AgCl (3 N KCl) reference electrode, to which the external potential, E, is referenced during the experiment. The potentials, however, are converted and referred against standard hydrogen electrode in the results. All measurements were performed in 50 mM H_2SO_4 solution (pH 1.05) using an SFA-2000 setup.[33] The optics of the SFA setup consisted of an imaging spectrometer (Shamrock 500) and a sCMOS detector (Zyla) from Andor.

The opposing surfaces were setup in a crossed-cylinder geometry,[32] with a nominal radius of curvature R = 2 cm. Measurements were done at 22 $\pm$ 0.5 °C, and only normal forces and normal shifts of the electrochemically active noble metal mirrors are reported in this study. For the measurement of the absolute distance, D, and the surface geometry, white light multiple beam interferometry was employed, which produces so-called fringes of equal chromatic order (FECO). The zero distance D_0 where D = 0 is given with respect to the mica|noble metal contact in dry nitrogen atmosphere. The absolute distance accuracy of our setup is better than 20−50 pm. For more details, the reader is referred to earlier work.[33] Throughout the article, we use the terms "positive (or negative) distance shift", which refers to the two mirrors used for optical measurement of ΔD moving away from (toward) each other; that is, D increases, hence ΔD is positive (and *vice versa* for "negative distance shifts").

The entire setup was placed on an isolation−vibration workbench, and additional weights were used to increase the load on the table close to the optimal load to minimize vibrations. Also, the experimental setup was placed in a temperature-controlled clean-room environment in a basement floor to minimize both building vibrations and thermal drift nominally to below 0.065 Å/s. In the data analysis, thermal drift was eliminated entirely by subtracting a linear first-order function from the data. In addition, thermal drift was also measured and found to be linear in most cases. Measurements with nonlinear drift due to sudden changes in the room temperature, or clearly visible vibrations of the building, were excluded from analysis. Typically, the thermal drift during a sweep experiment was well below 1−2 nm even for the slowest scan rates ($\geq$180 s total measurement time). The reported results have been measured with frame rates ranging from 2 to 10 frames per second, giving a time resolution of 500−100 ms. The system is theoretically capable of measuring frame rates up to 50−100 frames per second depending on the FECO intensities, which vary with the reflectivity of the used metal.

Conflict of Interest: The authors declare no competing financial interest.

Supporting Information Available: AFM topographies of all surfaces after experiment including statistical roughness evaluation, simulation of mirror shifts using the transfer matrix method, static oxide reduction for Au, Pt, and Pd, additional dynamic mirror shift plots for Pt, dynamic oxidation/reduction cycle for Au, current transients during static reduction/oxidation. This material is available free of charge *via* the Internet at http://pubs.acs.org.

REFERENCES AND NOTES

1. Etacheri, V.; Marom, R.; Elazari, R.; Salitra, G.; Aurbach, D. Challenges in the Development of Advanced Li-Ion Batteries: A Review. *Energy Environ. Sci.* **2011**, *4*, 3243−3262.
2. Simon, P.; Gogotsi, Y. Materials for Electrochemical Capacitors. *Nat. Mater.* **2008**, *7*, 845−854.
3. Markovic, N. M. Electrocatalysis Interfacing Electrochemistry. *Nat. Mater.* **2013**, *12*, 101−102.
4. Steele, B. C. H.; Heinzel, A. Materials for Fuel-Cell Technologies. *Nature* **2001**, *414*, 345−352.
5. Reier, T.; Oezaslan, M.; Strasser, P. Electrocatalytic Oxygen Evolution Reaction (OER) on Ru, Ir, and Pt Catalysts: A Comparative Study of Nanoparticles and Bulk Materials. *ACS Catal.* **2012**, *2*, 1765−1772.
6. Ghenciu, A. F. Review of Fuel Processing Catalysts for Hydrogen Production in PEM Fuel Cell Systems. *Curr. Opin. Solid State Mater. Sci.* **2002**, *6*, 389−399.
7. Frankel, G. S. Pitting Corrosion of Metals: A Review of the Critical Factors. *J. Electrochem. Soc.* **1998**, *145*, 2186−2198.
8. Alsabet, M.; Grden, M.; Jerkiewicz, G. Comprehensive Study of the Growth of Thin Oxide Layers on Pt Electrodes under Well-Defined Temperature, Potential, and Time Conditions. *J. Electroanal. Chem.* **2006**, *589*, 120−127.
9. Conway, B. E. Electrochemical Oxide Film Formation at Noble-Metals as a Surface-Chemical Process. *Prog. Surf. Sci.* **1995**, *49*, 331−452.
10. Grden, M.; Lukaszewski, M.; Jerkiewicz, G.; Czerwinski, A. Electrochemical Behaviour of Palladium Electrode: Oxidation, Electrodissolution and Ionic Adsorption. *Electrochim. Acta* **2008**, *53*, 7583−7598.
11. Reddy, A. K. N.; Genshaw, M. A.; Bockris, J. O. Ellipsometric Study of Oxygen-Containing Films on Platinum Anodes. *J. Chem. Phys.* **1968**, *48*, 671−675.
12. Klemm, S. O.; Karschin, A.; Schuppert, A. K.; Topalov, A. A.; Katsounaros, I.; Mayrhofer, K. J. J. Time and Potential Resolved Dissolution Analysis of Rhodium Using a Microelectrochemical Flow Cell Coupled to an ICP-MS (Vol 677, Pg 50, 2012). *J. Electroanal. Chem.* **2013**, *693*, 127−127.
13. Cherevko, S.; Topalov, A. A.; Katsounaros, I.; Mayrhofer, K. J. J. Electrochemical Dissolution of Gold in Acidic Medium. *Electrochem. Commun.* **2013**, *28*, 44−46.

14. Cherevko, S.; Topalov, A. A.; Zeradjanin, A. R.; Katsounaros, I.; Mayrhofer, K. J. J. Gold Dissolution: Towards Understanding of Noble Metal Corrosion. *RSC Adv.* **2013**, *3*, 16516–16527.

15. Klemm, S. O.; Karschin, A.; Schuppert, A. K.; Topalov, A. A.; Mingers, A. M.; Katsounaros, I.; Mayrhofer, K. J. J. Time and Potential Resolved Dissolution Analysis of Rhodium Using a Microelectrochemical Flow Cell Coupled to an ICP-MS. *J. Electroanal. Chem.* **2012**, *677*, 50–55.

16. Topalov, A. A.; Cherevko, S.; Zeradjanin, A. R.; Meier, J. C.; Katsounaros, I.; Mayrhofer, K. J. J. Towards a Comprehensive Understanding of Platinum Dissolution in Acidic Media. *Chem. Sci.* **2014**, *5*, 631–638.

17. Topalov, A. A.; Katsounaros, I.; Auinger, M.; Cherevko, S.; Meier, J. C.; Klemm, S. O.; Mayrhofer, K. J. J. Dissolution of Platinum: Limits for the Deployment of Electrochemical Energy Conversion? *Angew. Chem., Int. Ed.* **2012**, *51*, 12613–12615.

18. Duarte, M. J.; Klemm, J.; Klemm, S. O.; Mayrhofer, K. J. J.; Stratmann, M.; Borodin, S.; Romero, A. H.; Madinehei, M.; Crespo, D.; Serrano, J.; *et al.* Element-Resolved Corrosion Analysis of Stainless-Type Glass-Forming Steels. *Science* **2013**, *341*, 372–376.

19. Shrestha, B. R.; Nishikata, A.; Tsuru, T. Application of Channel Flow Double Electrode to the Study on Gold Dissolution during Potential Cycling in Sulfuric Acid Solution. *J. Electroanal. Chem.* **2012**, *665*, 33–37.

20. Shrestha, B. R.; Nishikata, A.; Tsuru, T. Channel Flow Double Electrode Study on Palladium Dissolution during Potential Cycling in Sulfuric Acid Solution. *Electrochim. Acta* **2012**, *70*, 42–49.

21. Shrestha, B. R.; Yadav, A. P.; Nishikata, A.; Tsuru, T. Application of Channel Flow Double Electrode to the Study on Platinum Dissolution during Potential Cycling in Sulfuric Acid Solution. *Electrochim. Acta* **2011**, *56*, 9714–9720.

22. Jerkiewicz, G.; Vatankhah, G.; Lessard, J.; Soriaga, M. P.; Park, Y. S. Surface-Oxide Growth at Platinum Electrodes in Aqueous H_2SO_4 Reexamination of Its Mechanism through Combined Cyclic-Voltammetry, Electrochemical Quartz-Crystal Nanobalance, and Auger Electron Spectroscopy Measurements. *Electrochim. Acta* **2004**, *49*, 1451–1459.

23. Edwards, M. Controlling Corrosion in Drinking Water Distribution Systems: A Grand Challenge for the 21st Century. *Water Sci. Technol.* **2004**, *49*, 1–8.

24. Gustafson, J.; Mikkelsen, A.; Borg, M.; Lundgren, E.; Kohler, L.; Kresse, G.; Schmid, M.; Varga, P.; Yuhara, J.; Torrelles, X.; *et al.* Self-Limited Growth of a Thin Oxide Layer on Rh(111). *Phys. Rev. Lett.* **2004**, *92*, 126102.

25. Lundgren, E.; Gustafson, J.; Resta, A.; Weissenrieder, J.; Mikkelsen, A.; Andersen, J. N.; Kohler, L.; Kresse, G.; Klikovits, J.; Biederman, A.; *et al.* The Surface Oxide as a Source of Oxygen on Rh(111). *J. Electron Spectrosc. Relat. Phenom.* **2005**, *144*, 367–372.

26. Lundgren, E.; Kresse, G.; Klein, C.; Borg, M.; Andersen, J. N.; De Santis, M.; Gauthier, Y.; Konvicka, C.; Schmid, M.; Varga, P. Two-Dimensional Oxide on Pd(111). *Phys. Rev. Lett.* **2002**, *88*, 246103.

27. Over, H.; Kim, Y. D.; Seitsonen, A. P.; Wendt, S.; Lundgren, E.; Schmid, M.; Varga, P.; Morgante, A.; Ertl, G. Atomic-Scale Structure and Catalytic Reactivity of the $RuO_2(110)$. *Surf. Sci.* **2000**, *287*, 1474–1476.

28. Wilms, M.; Broekmann, P.; Kruft, M.; Park, Z.; Stuhlmann, C.; Wandelt, K. STM Investigation of Specific Anion Adsorption on Cu(111) in Sulfuric Acid Electrolyte. *Surf. Sci.* **1998**, *402*, 83–86.

29. Renner, F. U.; Stierle, A.; Dosch, H.; Kolb, D. M.; Lee, T. L.; Zegenhagen, J. Initial Corrosion Observed on the Atomic Scale. *Nature* **2006**, *439*, 707–710.

30. Valtiner, M.; Banquy, X.; Kristiansen, K.; Greene, G. W.; Israelachvili, J. N. The Electrochemical Surface Forces Apparatus: The Effect of Surface Roughness, Electrostatic Surface Potentials, and Anodic Oxide Growth on Interaction Forces, and Friction between Dissimilar Surfaces in Aqueous Solutions. *Langmuir* **2012**, *28*, 13080–13093.

31. Israelachvili, J. N.; Kristiansen, K.; Gebbie, M. A.; Lee, D. W.; Donaldson, S. H., Jr.; Das, S.; Rapp, M. V.; Banquy, X.; Valtiner, M.; Yu, J. The Intersection of Interfacial Forces and Electrochemical Reactions. *J. Phys. Chem. B* **2013**, *117*, 16369–16387.

32. Valtiner, M.; Kristiansen, K.; Greene, G. W.; Israelachvili, J. N. Effect of Surface Roughness and Electrostatic Surface Potentials on Forces between Dissimilar Surfaces in Aqueous Solution. *Adv. Mater.* **2011**, *23*, 2294–2299.

33. Israelachvili, J.; Min, Y.; Akbulut, M.; Alig, A.; Carver, G.; Greene, W.; Kristiansen, K.; Meyer, E.; Pesika, N.; Rosenberg, K.; *et al.* Recent Advances in the Surface Forces Apparatus (SFA) Technique. *Rep. Prog. Phys.* **2010**, *73*, 036601.

34. Ying, C.; Schneider, P.; Bi-Ju, L.; Borodin, S.; Bin, R.; Erbe, A. Electronic Structure and Morphology of Dark Oxides on Zinc Generated by Electrochemical Treatment. *Phys. Chem. Chem. Phys.* **2013**, *15*, 9812–9822.

35. Israelachvili, J. N. *Intermolecular and Surface Forces*, 3ed ed.; Elsevier: New York, 2011.

36. Mayrhofer, K. J. J.; Meier, J. C.; Ashton, S. J.; Wiberg, G. K. H.; Kraus, F.; Hanzlik, M.; Arenz, M. Fuel Cell Catalyst Degradation on the Nanoscale. *Electrochem. Commun.* **2008**, *10*, 1144–1147.

37. Ferreira, P. J.; la O', G. J.; Shao-Horn, Y.; Morgan, D.; Makharia, R.; Kocha, S.; Gasteiger, H. A. Instability of Pt/C Electrocatalysts in Proton Exchange Membrane Fuel Cells: A Mechanistic Investigation. *J. Electrochem. Soc.* **2005**, *152*, A2256–A2271.

38. TremiliosiFilho, G.; DallAntonia, L. H.; Jerkiewicz, G. Limit to Extent of Formation of the Quasi-Two-Dimensional Oxide State on Au Electrodes. *J. Electroanal. Chem.* **1997**, *422*, 149–159.

39. Tremiliosi-Filho, G.; Dall'Antonia, L. H.; Jerkiewicz, G. Growth of Surface Oxides on Gold Electrodes under Well-Defined Potential, Time and Temperature Conditions. *J. Electroanal. Chem.* **2005**, *578*, 1–8.

40. Horn, R. G.; Smith, D. T. Analytic Solution for the 3-Layer Multiple Beam Interferometer. *Appl. Opt.* **1991**, *30*, 59–65.

41. Levins, J. M.; Vanderlick, T. K. Extended Spectral-Analysis of Multiple-Beam Interferometry: A Technique To Study Metallic-Films in the Surface Forces Apparatus. *Langmuir* **1994**, *10*, 2389–2394.

42. Wu, X.; Erbe, A.; Raabe, D.; Fabritius, H. O. Extreme Optical Properties Tuned through Phase Substitution in a Structurally Optimized Biological Photonic Polycrystal. *Adv. Funct. Mater.* **2013**, *23*, 3615–3620.

43. Erbe, A. Simulation of Infrared and UV/Vis Reflectance and Transmission Spectra of Stratified Systems; http://home.arcor.de/aerbe/en/prog/a/reflcalc20140411/reflcalc20140411.html.

44. Takeuchi, A.; Takeuchi, N. Electrical Changes in Pre- and Postsynaptic Axons of Giant Synapse of Loligo. *J. Gen. Physiol.* **1962**, *45*, 1181–1193.

45. Kristiansen, K.; Valtiner, M.; Greene, G. W.; Boles, J. R.; Israelachvili, J. Pressure Solution: The Importance of the Electrochemical Surface Potentials. *Geochim. Cosmochim. Acta* **2011**, *75*, 6882–6892.

46. Todorova, M.; Neugebauer, J. Extending the Concept of Defect Chemistry from Semiconductor Physics to Electrochemistry. *Phys. Rev. Appl.* **2014**, *1*, 014001–014015.

47. Marenduzzo, D.; Finan, K.; Cook, P. R. The Depletion Attraction: An Underappreciated Force Driving Cellular Organization. *J. Cell Biol.* **2006**, *175*, 681–686.

48. Sprague, I. B.; Byun, D.; Dutta, P. Effects of Reactant Crossover and Electrode Dimensions on the Performance of a Microfluidic Based Laminar Flow Fuel Cell. *Electrochim. Acta* **2010**, *55*, 8579–8589.